



Full Length Article

Ionic transport in Samarium doped Ceria free-standing single crystal membrane

Simone Sanna^{a,*}, Olga Krymskaya^a, Zhongtao Ma^b, Salvatore De Angelis^b, Daniele Di Castro^a, Roberto Felici^c, Alessandro Coati^d, Giuseppe Balestrino^a, Søren Bredmose Simonsen^b, Antonello Tebano^a

^a CNR-SPIN and Department of Civil Engineering and Computer Science, University of Rome Tor Vergata, I-00133 Rome, Italy

^b Department of Energy Conversion and Storage, Technical University of Denmark, Fysikvej, Building 310, DK-2800 Kgs. Lyngby, Denmark

^c CNR-SPIN, Via Del Fosso del Cavaliere 100, I-00133 Rome, Italy

^d Synchrotron SOLEIL, L'Orme des Merisiers, F-91190 Saint-Aubin, France

ARTICLE INFO

Keywords:

Micro-Solid Oxide electrochemical cells
Pulsed Laser Deposition (PLD)
Free-standing membrane
Samarium doped ceria (SDC)
Sacrificial layer

ABSTRACT

We present the realization of Samarium Doped Ceria (SDC) free-standing membranes and their structural and ionic transport properties. An epitaxial layer of water-soluble Sr₃Al₂O₆ (SAO) sacrificial layer was deposited onto SrTiO₃ (100) oriented single crystal substrate, followed by the deposition of the SDC layer. The free-standing SDC membrane was produced by etching the SAO layer in water. The creation of a 2D free-standing membrane allowed us to determine its transport and structural properties without any possible contribution of the substrate. Moreover, the availability of a thin SDC single crystal free-standing membrane offers the opportunity to tune the electrical properties by applying, for instance, compressive or tensile strain much larger than any substrates can induce by the lattice mismatch. Furthermore, this procedure allows the transfer of the film onto any kind of substrate and complex integrated circuit, i.e. those based on silicon technologies, giving the possibility to realize a new class of complex devices based on oxide ultra-thin films.

1. Introduction

The capability to produce, manipulate and integrate thin films and heterostructures of complex two-dimensional oxides in devices might have a great impact on thin film based technologies. The increasing demand for portable and miniaturized devices for energy storage and conversion makes the development of thin film technologies, with the scope to fabricate micro electrochemical devices such as micro-Solid Oxide Fuel Cells (mSOFCs) and micro-Solid Oxide Electrochemical Cells (mSOECs), urgent [1–4]. These electrochemical cells, based on layers (electrolyte/cathode/anode) a few nanometers thick, exhibit many advantages, i.e. high specific energy per unit of volume, lower operative temperatures, flexibility to integrate them in a new generation of advanced multifunctional devices based on oxide materials [5–8].

Pulsed Laser Deposition (PLD) is one of the most suitable deposition techniques used to deposit, onto single crystal substrate, oxide thin films and heterostructures with excellent crystallographic quality. However, due to the deposition conditions (high temperature and high oxygen partial pressure), the integration in complex devices of thin films grown

by PLD still presents unresolved problems.

Very often the main limitation in the application of films and heterostructures of complex oxides, made by PLD, to fabricate devices, is strictly related to the presence of the substrate on which the film was deposited.

The substrate has not only the function of mechanical support, but often stabilizes, otherwise unstable, phases through structural and chemical compatibility with the film. The high crystallographic quality of the films produced by PLD is closely related to the substrate. The choice of the substrate is mostly guided by the in-plane lattice match with the material to be deposited. In most cases, it will be the crystallographic order induced by the substrate to determine the chemical-physical properties of the film. The presence of the substrate, used for deposition, represents the main constraint that generally prevents the integration of the PLD-realized films or heterostructures in devices of possible application interest. Therefore, it is important to combine the ability offered by PLD, to produce films of materials with new or improved physical properties, with different kinds of supporting substrates already integrated with more complex circuits. Nowadays, in

* Corresponding author.

<https://doi.org/10.1016/j.mtla.2023.101836>

Received 20 March 2023; Accepted 23 June 2023

Available online 23 June 2023

2589-1529/© 2023 The Authors. Published by Elsevier B.V. on behalf of Acta Materialia Inc. This is an open access article under the CC BY license (<http://creativecommons.org/licenses/by/4.0/>).

various applications for microelectrochemical systems, it is also crucial to make available free-standing membranes to achieve a high level of integration with silicon technologies. Furthermore, for many devices high mechanical flexibility, is often required, which cannot be obtained in the presence of a substrate. Different microelectrochemical cell designs, reported in the literature, are based on free-standing electrolyte membranes deposited onto silicon substrates [9–12].

In the last decade doped Ceria, has been considered a very promising candidate as a component for the SOFCs and SOECs because of its large ionic conductivity and remarkable stability in reducing conditions [13, 14]. Indeed, doped ceria, with Ce^{+4} replaced by trivalent cations such as Gd^{+3} or Sm^{+3} represents an up-and-coming class of electrocatalytic materials to reduce carbon dioxide at high temperatures. Recent studies also show a considerable ability of doped Ceria to reduce CO_2 by electrolysis [14]. Moreover, in contrast to Ni-based materials which tend to degrade, the catalytic properties of ceria are very stable over time despite the carbon production on the surface of the electrolyte during operation at high temperatures [2]. Recently it has been demonstrated that its electronic and ionic conductivity could be tuned and enhanced under light radiation in the near-UV [2]. Moreover, doped ceria exhibits good performances for photo-catalysis and a remarkable carbon-deposition suppression capability [14,15].

In this paper, we report on the realization of samarium doped ceria (SDC) free-standing membrane deposited by PLD with in-situ RHEED characterization. We investigated the crystallographic properties of the SDC free-standing membrane by X-Ray Diffraction also using synchrotron radiation. By Electrochemical Impedance Spectroscopy (EIS) integrated with Transmission Electron Microscopy (TEM), we investigated the electrochemical and structural properties of SDC free-standing membranes.

2. Materials and methods

To fabricate SDC free-standing membranes, epitaxial SDC and SAO were grown by PLD onto a STO (001) oriented substrate: the growth conditions of the two layers were optimised to improve their crystallographic quality. The substrate was subsequently detached by the SDC film, dissolving the sacrificial SAO layer in distilled water. The film deposition was carried out using a KrF excimer laser (248 nm wavelength, pulse width 25 ns). The laser beam, with an energy per pulse of 100 mJ, was focused, in a high vacuum chamber, onto a target with an energy density per laser pulse of about 3 J/cm^2 .

The first step before depositing the SAO/SDC heterostructures was to optimize the deposition conditions of both SAO and SDC compounds. The optimized deposition temperature for the SAO layer was 750°C , and the O_2 atmosphere background pressure in the chamber was fixed to 10^{-4} mbar. The optimized deposition temperature for the SDC layer was 700°C and the O_2 partial pressure in the chamber was fixed to 10^{-1} mbar.

The growth mechanism of SAO and SDC films was monitored by in situ reflection high energy electron diffraction (RHEED) diagnostics: electron gun operating at 15KV and 1.5 A.

θ – 2θ XRD scans and rocking curve analysis were performed using a Rigaku diffractometer having a Cu anode as X-ray source operating at 25 KV and 15 mA. Grazing Incidence X-ray Diffraction (GIXD), Crystal Truncation Rods (CTR) and X-ray Reflectivity (XRR) measurements were performed at synchrotron SOLEIL SixS (Surfaces interfaces X-ray Scattering) beamline.

For the SEM-EDS analysis, the sample underwent analysis using the advanced Zeiss Ultra scanning electron microscope (SEM) with a field emission gun, which was equipped with an energy-dispersive X-ray spectrometer (EDS). The microscope was operated at an accelerating voltage of 15 keV and a working distance of 8.5 mm. The spectral peaks generated from the EDS analysis were identified and assigned to the following characteristic X-ray lines: Pt $\text{M}\alpha\beta$, Ce $\text{L}\alpha$, and O K.

Electrochemical Impedance Spectroscopy (EIS) was carried out in air

on the SDC free-standing membrane at DTU, Energy department. EIS was performed with a 20 mV alternating voltage signal in the $500\text{--}800^\circ\text{C}$ temperature range and 0.1Hz–0.1 MHz frequency range, respectively.

SAO/SDC heterostructures were deposited by PLD onto a $5 \times 5 \times 0.5 \text{ mm}^3$ STO (001) single crystal.

A layer of adhesive polymer (PDMS Gelpack) was applied onto the surface of the final SDC layer. The PDMS/SDC/SAO/STO system was then immersed in water at room temperature and the SAO sacrificial layer dissolved. In such a way, after few hours, the film SDC was transferred onto PDMS. We accomplished the transfer of the SDC layer from PDMS to Si by simply placing the PDMS/SDC structure onto a Si wafer. This transfer process was completed within a few hours.

3. Results and discussion

Fig. 1a shows a typical θ – 2θ XRD diffraction pattern of a SDC film deposited onto a STO(001) substrate. Only (00 L) diffraction peaks of the SDC fluorite structure and STO perovskite structure are evident. This proves the c-axis oriented growth of the SDC film onto the STO substrate.

The mosaic spread, measured by the Full Width at Half Maximum (FWHM) of the ω scan around the (002) SDC reflection (Fig. 1b), resulted to be 0.7° . This low mosaic spread value indicates the good crystallographic quality of SDC films deposited directly onto the STO substrate.

Fig. 1c and 1d show the x-ray diffraction patterns in θ – 2θ and ω scan mode (rocking curve) of the SDC/SAO/STO(001) heterostructure respectively.

In the θ – 2θ scan, the presence of the SDC, STO, and SAO (00 L) peaks, unequivocally indicates the c-axis orientation of the entire heterostructure.

The ω scan around the SDC (002) reflection exhibits a value of FWHM of about 0.4° . This value is smaller than the value obtained for the SDC film deposited directly onto the STO substrate. This result indicates the good crystallographic quality of the SAO layer as well. The SAO has a lattice parameter very similar to a multiple of the one of STO. As a consequence, its diffraction peaks, observable with a standard laboratory diffractometer, are superimposed onto the STO peaks and it was not possible to measure the SAO mosaic spread using ω scans.

From the fit of XRD finite size effect oscillations around the (002) SDC peak in the SDC/SAO/STO(001) heterostructure (Fig. 1e), the deposition rate was determined. The deposition rate resulted to be about 0.14 \AA/pulse and the SDC layer thickness estimated for the SDC/SAO heterostructure was about 14 nm. The peak at $2\theta = 31.64^\circ$ is the SAO (006) reflection.

To obtain a possible integration of ceria films in devices based on silicon technologies, for the fabrication of micro-Solid Oxide Electrochemical cells (micro-SOEC) and micro-Solid Oxide Fuel Cells (micro-SOFC), the surface quality of the different layers involved is of fundamental importance. Fig. 2 shows the Reflection High Energy Electron Diffraction (RHEED) pattern evolution during the different steps of the heterostructure PLD growth. Fig. 2a shows a typical RHEED pattern of the STO (001) single crystal. Fig. 2b displays a typical RHEED pattern obtained after a few unit cells of the SAO sacrificial layer deposition. Fig. 2c shows the RHEED pattern of the SAO layer at the end of the growth after 5000 laser shots; the streaky pattern indicates a smooth, almost 2D, SAO surface. After the deposition of a few SDC unit cells onto the SAO, the diffraction pattern exhibits a 3D growth indicating the presence of defects at the SDC/SAO interface, likely induced by the lattice mismatch (Fig. 2d). However, after the deposition of SDC layer, 2–3 nm thick, the RHEED pattern again showed, a streaky pattern due to the evolution from a 3D to a quasi 2D growth for the SDC (Fig. 2e).

The SDC/SAO/STO heterostructure was then immersed in distilled water to dissolve the SAO layer and detach the SDC layer from the STO substrate. Fig. 3a shows the θ – 2θ diffraction pattern of the free-standing SDC film transferred onto polymer PDMS Gelpack. In the diffraction pattern, only the (002) peak of the SDC is present, confirming the

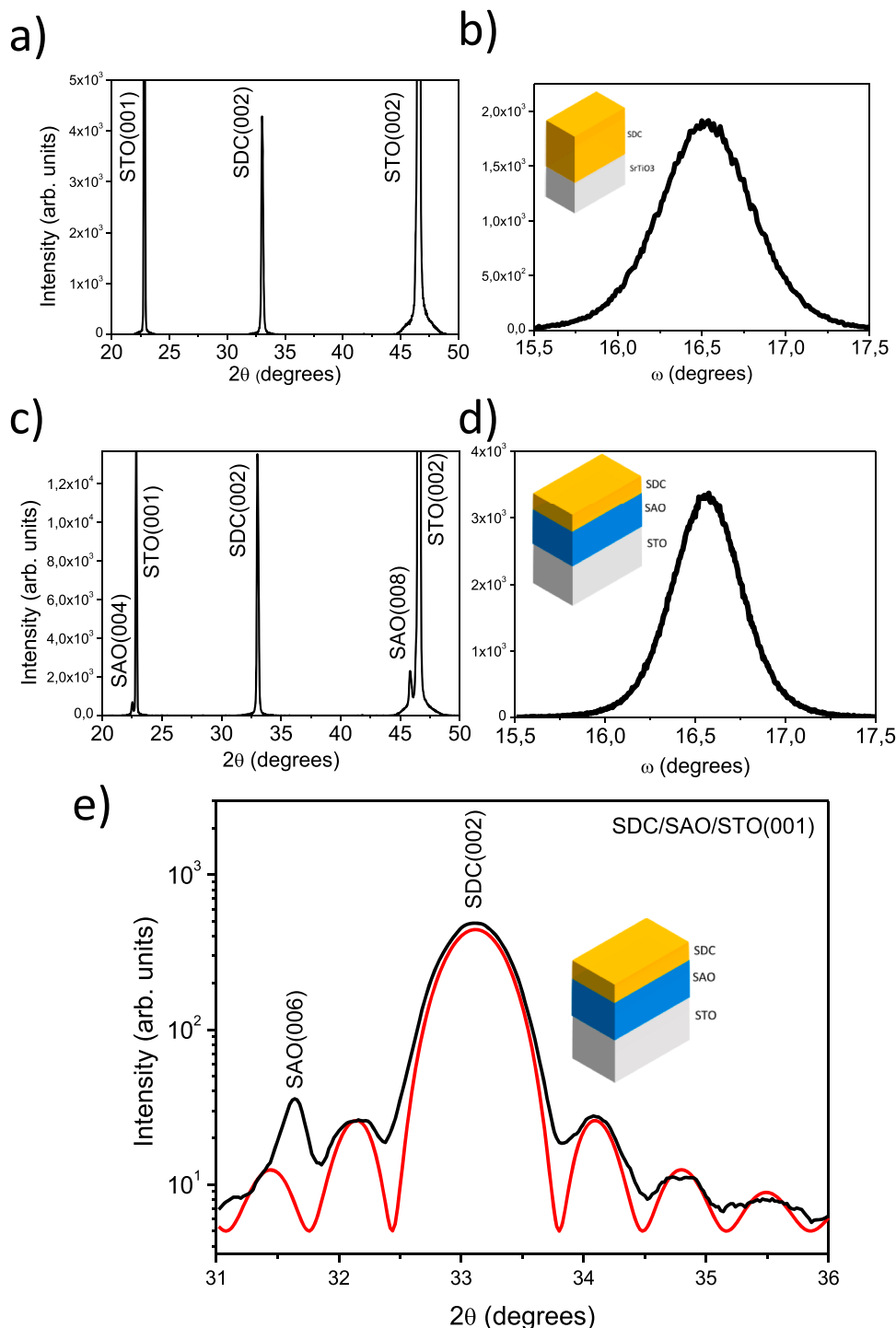


Fig. 1. XRD patterns in θ - 2θ and ω (rocking curve) scan mode respectively: SDC/STO a) and b), SDC/SAO/STO c) and d). XRD patterns in θ - 2θ scan mode of SDC/SAO/STO with size effect fit in red around the (002) SDC peak e).

successful transfer of the film onto the flexible polymer PDMS. Fig. 3b shows the rocking curve of the free-standing SDC membrane onto the flexible polymer: the FWHM value of the (002) reflection in the ω scan resulted to be about 1.5° . This value is larger than the value obtained for the SDC film in the heterostructure. Such a large value of the rocking curve has to be ascribed to the not perfect planarity of the SDC film on the PDMS polymer. Fig. 3c reports the θ - 2θ diffraction pattern of the SDC film, transferred from the polymer onto the silicon substrate: only the (002) peak of the SDC in the diffraction pattern is noticeable. The rocking curve around the (002) SDC reflection, showed a FWHM value

of 0.7° (Fig. 3d). This value similar to the value obtained for the heterostructure SDC/SAO/STO, confirms that the larger value measured in the case of the SDC film onto the PMMA was essentially due to the bending of the flexible SDC free-standing membrane.

From the (002) SDC peak position in the θ - 2θ x-ray diffraction pattern, the out-of-plane lattice parameter results to be $c = 5.42 \text{ \AA}$ for either the SDC/STO(001) (Fig. 1a), SDC/SAO/STO(001) (Fig. 1c), and SDC/PDMS (Fig. 3a). However, the film transferred onto Si has an out of plane lattice parameter slightly larger ($c = 5.50 \text{ \AA}$) than that previously observed for the SDC/STO and SDC/SAO/STO(001) heterostructure

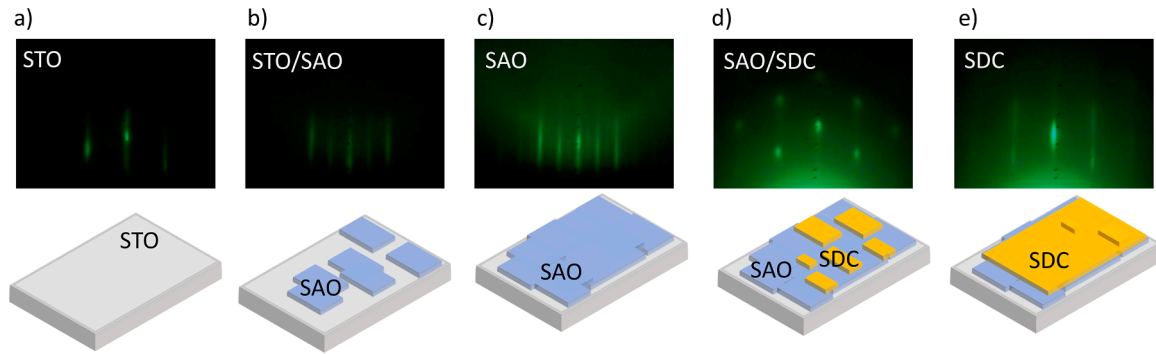


Fig. 2. The Reflection High Energy Electron Diffraction (RHEED) pattern evolution during the different steps of the heterostructure realization: STO (100) single crystal a); during SAO deposition b) and c); during SDC deposition d) and e).

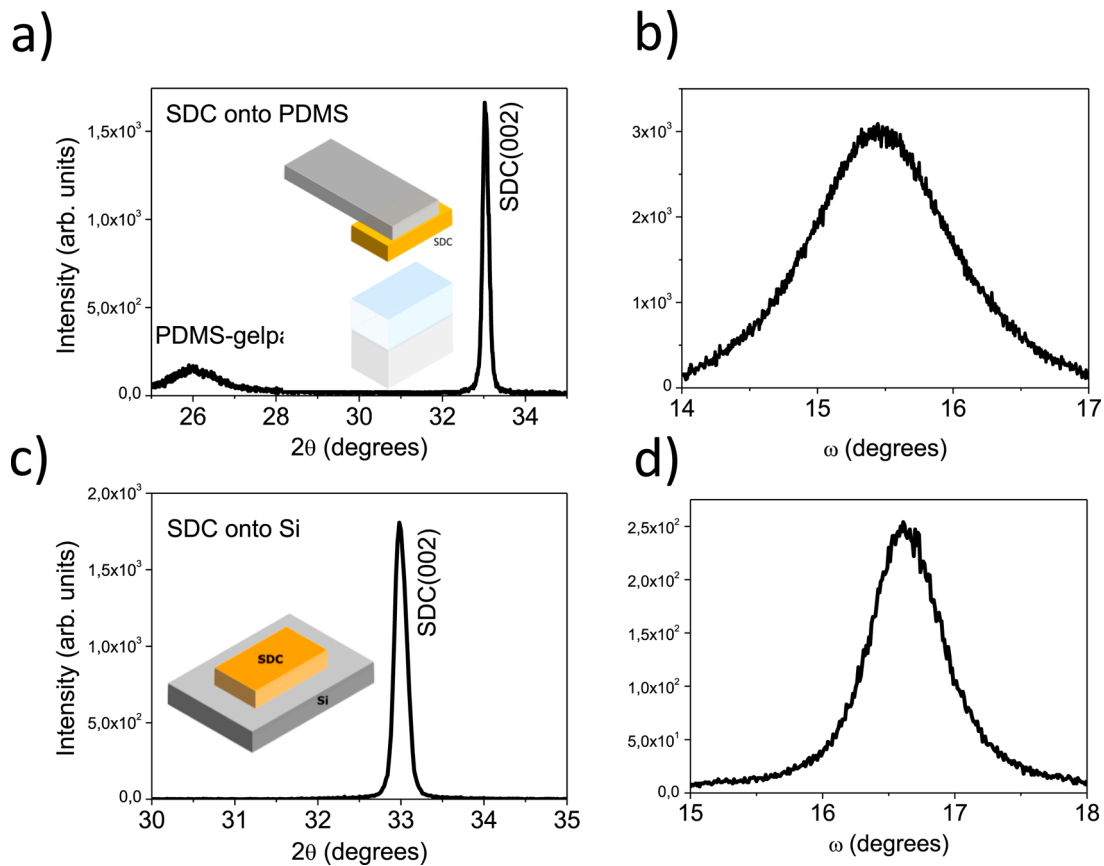


Fig. 3. XRD patterns in θ – 2θ and ω (rocking curve) scan mode respectively: SDC onto PDMS a) and b), SDC onto Si c) and d).

(Fig. 3c). Such a larger lattice parameter, close to the fully relaxed c value, can be ascribed to the absence of tensile strain in the fluorite cubic cell when the film is reported onto Si substrate.

To have a better insight into the crystalline structure of the SDC heterostructures and free-standing membranes, surface x-ray diffraction measurements (SXRD) have been carried out at the SIXS beamline of the SOLEIL synchrotron facility in Paris, France. The synchrotron radiation allowed us to perform high-resolution XRD measurements with an enhanced sensitivity. Fig. 4 reports the in-plane Reciprocal Space Map (RSM) in reciprocal lattice units (r.l.u.) for two SDC/SAO/STO(001) heterostructures differing in the thickness of the SDC layer. As a reference, we used the reciprocal lattice of the STO cubic lattice, in which the reciprocal space unit vectors a^* , b^* and c^* are parallel to the a , b and c vectors defining the cubic unit cell and have a magnitude equal to $2\pi/a_0$, where $a_0 = 3.905 \text{ \AA}$ is the lattice parameter of the STO. In the coordinate

system we used, the a^* and b^* vectors lie on the sample surface while the c^* vector is perpendicular to it. The diffraction vectors H , K and L are parallel to the a^* , b^* and c^* vectors respectively. Fig. 4a refers to the case where the thickness of the SDC layer is 70 nm while, in Fig. 4b, the thickness is 14 nm. Similarly, Fig. 4c and d show the data collected for SDC free-standing membrane with thicknesses of 70 nm and 14 nm respectively. The RSMs were collected at a vertical exchanged momentum of $L = 0.7 \text{ r.l.u.}$ We chose this value to limit the intensity of the substrate peaks, which are in fact not visible in the figures, and to maximize the intensity of the SAO and SDC peaks. The observable peaks in Fig. 4 belong either to the SAO layer or to the SDC film. Under the assumption that the heterostructure is perfectly commensurate, we can index all the reflections using the following basis for the SDC and the SAO:

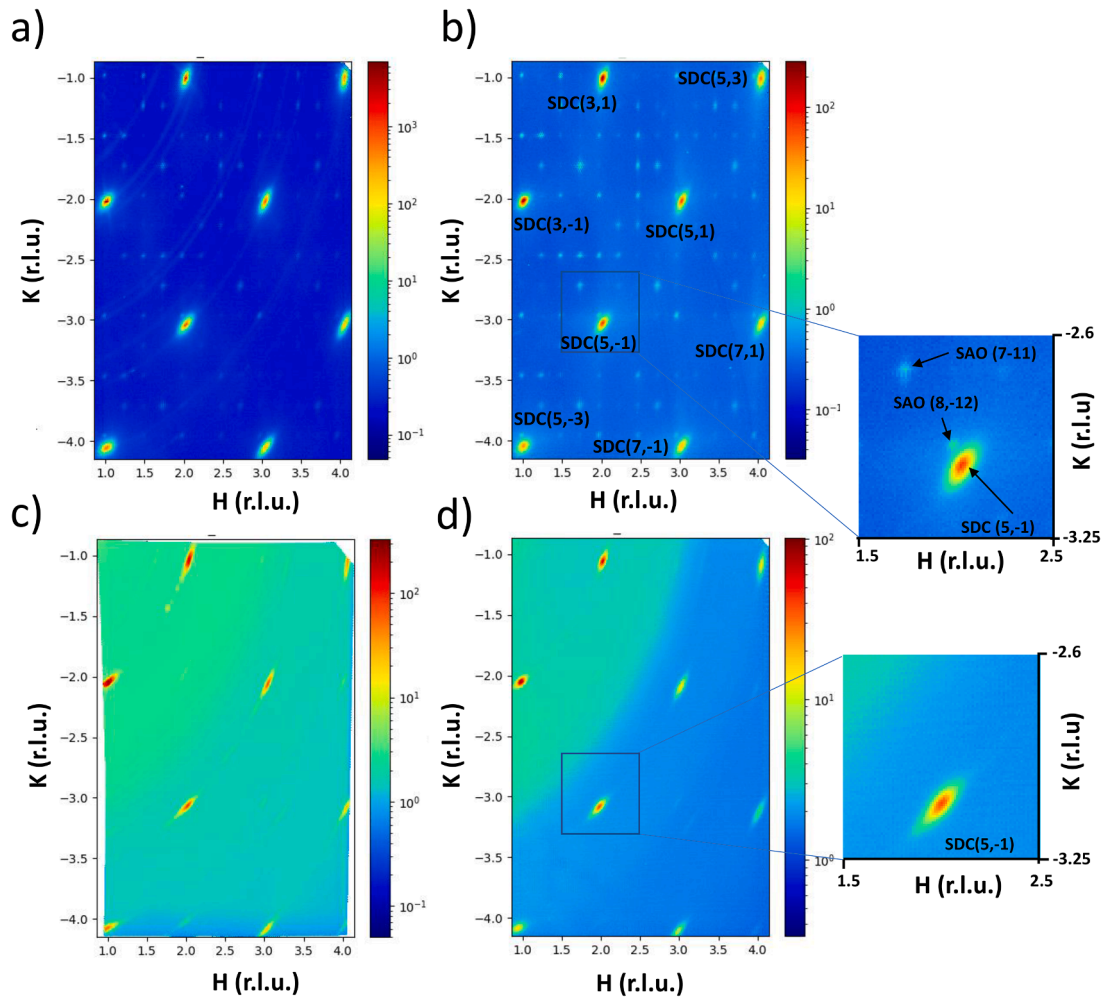


Fig. 4. In-plane Reciprocal Space Map (RSM) in reciprocal lattice units (r.l.u.) for the heterostructures SDC/SAO/STO(001) having SDC thickness of 70 nm and 14 nm respectively (a, b) and for the SDC free-standing membrane with thicknesses of 70 nm and 14 nm respectively (c, d). The RSMs have been collected at a vertical exchanged momentum of $L = 0.7$ r.l.u.

$$\mathbf{a}^* = \mathbf{a}_{SDC}^* + \mathbf{b}_{SDC}^* ; \mathbf{b}^* = -\mathbf{a}_{SDC}^* + \mathbf{b}_{SDC}^*$$

$$\mathbf{a}^* = 4\mathbf{a}_{SAO}^* ; \mathbf{b}^* = 4\mathbf{b}_{SAO}^*$$

In the RSMs reported in Fig. 4, several series of peaks belonging to the SAO layer and SDC film, respectively, are clearly observable. In Fig. 4b the peaks corresponding to the SAO layer are more evident due of

the reduced thickness of the SDC layer.

The RSMs give the opportunity of appreciating the structural quality of the heterostructures. Only one phase is observable for both the SAO and SDC, whose lattices appear to be fully relaxed. Fig. 4c and d prove that the structure of the SDC free-standing membranes remains almost unchanged during the transfer process.

The inset of Fig. 4b allows to make a further discussion on the

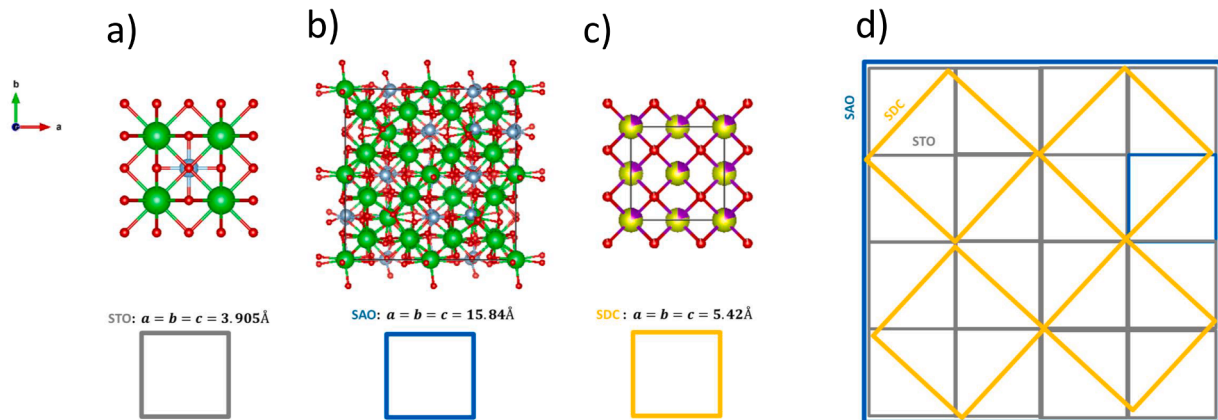


Fig. 5. Epitaxial relationship between SDC fluorite ($a_{SDC} = 5.42\text{Å}$), STO perovskite ($a_{STO} = 3.905\text{Å}$) and SAO ($a_{SAO} = 15.82\text{Å}$) with space group ($Pa\bar{3}$).

structure of the different layers in the heterostructure. The STO substrate has a cubic perovskite structure with a lattice parameter of $a_{\text{STO}} = 3.905$ Å the lattice of SDC is fluorite cubic with $a_{\text{SDC}} = 5.42$ Å, while SAO is cubic, spec group $Pa\bar{3}$ with a lattice parameter of 15.84 Å. These apparently very different values in the lattice parameters correspond indeed to very well matched structures as explained in Fig. 5, where the atomic positions are outlined. The lattice parameter of STO has then to be compared with one-fourth of the one of SAO ($15.84/4 = 3.96$ Å) and to half of the diagonal of the SDC lattice ($\frac{5.42}{\sqrt{2}} = 3.83$ Å). It is then clear that all the structures are very well matching each other with an average difference of about 2%.

The fabrication of a free-standing membrane has given us the possibility to measure unambiguously the conductivity of a thin SDC film without any possible contribution provided by the substrate. With this aim, the SDC free-standing membrane was studied by Electrochemical Impedance Spectroscopy (EIS) and Scanning Electron Microscopy - Energy Dispersive Spectrometry (SEM-EDS) using a state-of-the-art system. Fig. 6a shows the SEM image of the flake of the SDC free-standing membrane mounted on two Pt electrodes of the chip. The red circles indicate the positions of the connections made of ion-deposited Pt between the SDC flake and the chip electrodes (Fig. 6a). The corresponding SEM-EDS maps of Pt, Ce, and O show the positions of the sample in the chip (Fig. 6b, c, d). Fig. 6e shows the EIS spectra recorded at 700 °C, 750 °C, and 800 °C. The two conventional arcs are shown in all spectra. The first arc is due to the ohmic transport through the SDC flake denoted by R_t in the electrical circuit model (ECM) (see the zoom inset in Fig. 6e). CPE_{shunt} is the shunt capacitance, originated from the instruments used for the electric test such as: the electrical circuit on the MEMS chip, the TEM holder, and the cables connecting to the potentiostat. This instrument contribution is in parallel to all sample contributions and causes the first arc to start from 0. The second arc in Fig. 6c can be ascribed to the surface exchange reactions at the triple phase boundaries between O_2 , SDC and Pt electrodes, including the surface reaction resistance R_p and the interface capacitance CPE_{int} between the O_2 and SDC surface.

Fig. 7 shows the Arrhenius plots of the electrical conductivity in the 500–800 °C temperature range in air for a SDC free-standing membrane having a total thickness of about 180 nm as indicated by the electron energy loss spectroscopy measurements. Fig. 7 also shows the Arrhenius plot of a SDC pellet and STO-buffered SDC film (SDC/STO/MgO(001)) for comparison [13,16]. Considering the difficulties to estimate the cell parameter, due to the irregular shape of the flake and to the geometry of the contacts (Fig. 6a), we can say that the total conductivity of the SDC free-standing membrane follows substantially the behavior data

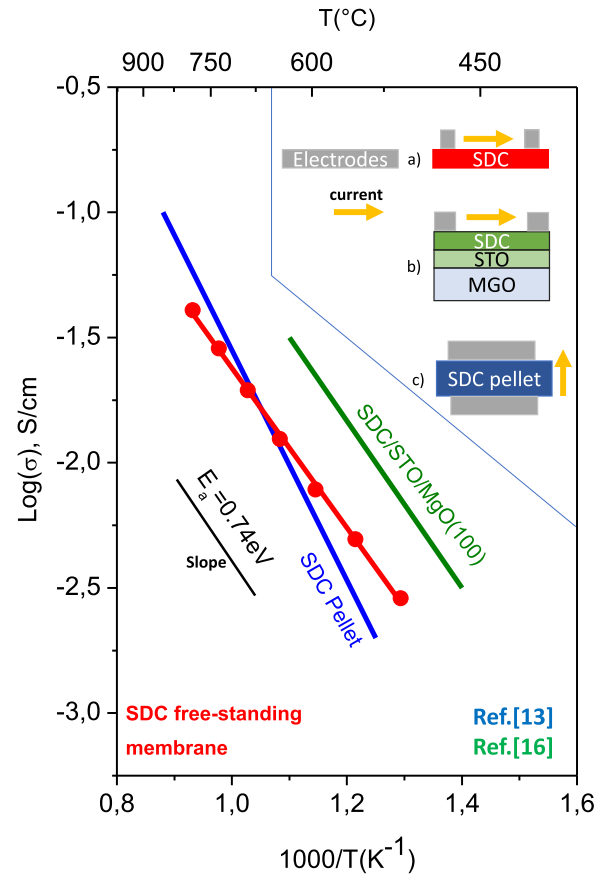


Fig. 7. Arrhenius plot of electrical conductivity measured in the 500–800 °C temperature range in air for a SDC free-standing membrane (red dots); SDC/STO/MgO (green line, ref. [16]); SDC pellet (blue line ref. [13]). In the inset schematic sketch of the geometric three configurations of the electrical measurements for a) free-standing membrane, b) SDC/STO/STO(001) and SDC pellet.

reported in the literature for the SDC pellet [5,13]. The activation energy results to be about $E_a = 0.64$ eV. Such a value is smaller than the value reported in the literature for a SDC polycrystalline pellet [13]. On the contrary, it is very close to the value of 0.74 eV previously reported for SDC single crystal thin film [16]. The similarity of the activation

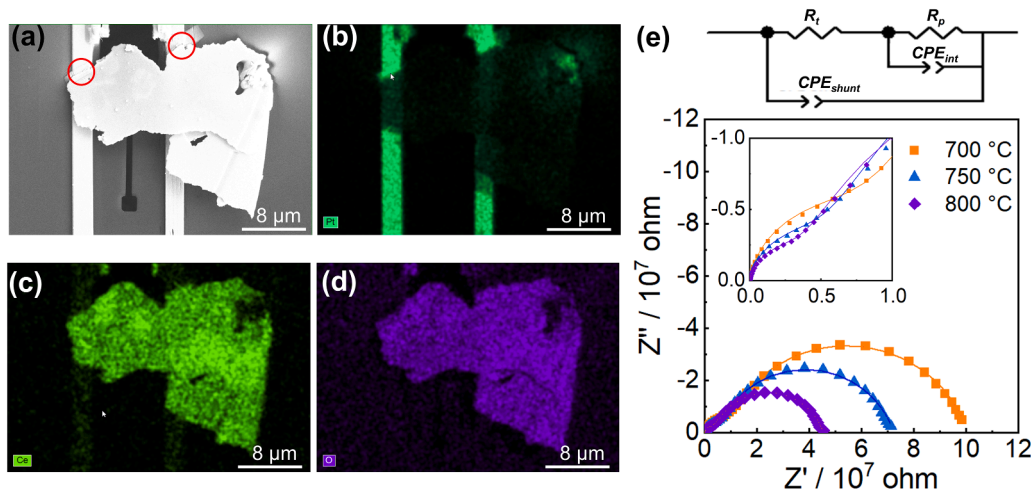


Fig. 6. (a) SEM image of a Sm-doped ceria sample. The corresponding SEM-EDS map is displayed in (b), with the Pt $M\alpha$ peak indicated, in (c), with the Ce $L\alpha$ peak, and in (d), with the O $K\alpha$ peak. The positions of the Pt connections are indicated by two red circles (a). The Pt connections were made by FIB-SEM ion-beam deposition. The EIS spectra at 700 °C, 750 °C, and 800 °C, with the corresponding electric model circuit, are shown in (e).

energy value between the SDC free-standing membrane and that one of the epitaxial thin film single crystal, both smaller than that of the SDC pellet, is ascribed to the absence of grain boundaries in both cases. The observed lower value in the conductivity of the free-standing membrane compared to that of the film onto the substrate can be ascribed to the absence of any contribution to the conductivity coming from the substrate.

4. Conclusions

In this work we showed that it is possible to fabricate free-standing membranes of doped ceria having thicknesses in the range from 14 nm to 180 nm with excellent crystallographic quality. Furthermore, we have shown the possibility to transfer the SDC layer onto Si substrate maintaining the good crystallographic quality of the film.

In polycrystalline doped ceria, the ionic conductivity depends on microstructural parameters such as grain boundaries. For instance, a reduction of ionic conductivity has been observed with an increasing number of grain boundary regions per unit length [13]. The increase of the resistance can be ascribed to the segregation of the dopants, the presence of impurities, and the concentration of point defects at the grain boundaries. These occurrences act like blocking layers for the ionic charge carriers resulting in an increase of the activation energy.

Electrochemical Impedance Spectroscopy measurements in the 500°–800 °C temperature range were carried out successfully on the SDC flake giving an activation energy value, calculated from the Arrhenius plot, similar to that of the SDC single crystal, and lower than that of the SDC polycrystalline [13].

The lower value of the activation energy obtained for the epitaxial SDC flake, compared to that one of the SDC pellet, can be ascribed to the absence of grain boundary regions, as a consequence of the depletion of electronic charge carriers with the increasing of the crystallographic quality of the film.

The process we described can be employed for the integration of ceria thin film in devices based on silicon technologies with the aim to develop a new class of micro-Solid Oxide Electrochemical cells, micro-Solid Oxide Fuel Cells, and, more general multifunctional iono-electronic devices. Moreover, the possibility to transfer ultrathin SDC films onto other oxide surfaces with tailored oxide terminations might open new strategies to engineer the interfaces of the heterostructures with novel properties.

The transport properties of oxide thin films, such as ionic [5], electronic conductivity [17], and super-conductivity [18,19], can be tuned and enhanced by the strain. Free-standing membranes could also open new possibilities for integration in complex MEMS sensors and devices.

Declaration of Competing Interest

The authors declare that they have no known competing financial interests or personal relationships that could have appeared to influence the work reported in this paper.

Acknowledgement

This project has received funding from:

- The European Research Council (ERC) under the European Union's Horizon 2020 research and innovation program (grant agreement No 850850)
- Regione Lazio "Lazio Innova", MATeriali avanzati Riconversione CO₂ via adsorbimento su sistemi Larga area di contratto (MATRICOLA) (CUP: B85F21001230005)

References

- [1] A. Hauch, R. Küngas, P. Blennow, A.B. Hansen, J.B. Hansen, B.v. Mathiesen, M. B. Mogensen, Recent advances in solid oxide cell technology for electrolysis, *Science* 370 (2020) (1979), <https://doi.org/10.1126/science.aba6118>.
- [2] M.B. Mogensen, M. Chen, H.L. Frandsen, C. Graves, J.B. Hansen, K.v. Hansen, A. Hauch, T. Jacobsen, S.H. Jensen, T.L. Skafte, X. Sun, Reversible solid-oxide cells for clean and sustainable energy, *Clean Energy* 3 (2019) 175–201, <https://doi.org/10.1093/ce/zkz023>.
- [3] M. Coll, J. Fontcuberta, M. Althammer, M. Bibes, H. Boschker, A. Calleja, G. Cheng, M. Cuoco, R. Dittmann, B. Dkhil, I. el Baggari, M. Fanciulli, I. Fina, E. Fortunato, C. Frontera, S. Fujita, V. Garcia, S.T.B. Goennenwein, C.G. Granqvist, J. Grolier, R. Gross, A. Hagfeldt, G. Herranz, K. Hono, E. Houwman, M. Huijben, A. Kalaboukhov, D.J. Keeble, G. Koster, L.F. Kourkoutis, J. Levy, M. Lira-Cantu, J. L. MacManus-Driscoll, J. Mannhart, R. Martins, S. Menzel, T. Mikolajick, M. Napari, M.D. Nguyen, G. Niklasson, C. Paillard, S. Panigrahi, G. Rijnders, F. Sánchez, P. Sanchis, S. Sanna, D.G. Schlom, U. Schroeder, K.M. Shen, A. Siemon, M. Spreitzer, H. Sukegawa, R. Tamayo, J. van den Brink, N. Pryds, F.M. Granozio, Towards oxide electronics: a roadmap, *Appl Surf Sci.* 482 (2019) 1–93, <https://doi.org/10.1016/j.apsusc.2019.03.312>.
- [4] Y. Shi, I. Garbayo, P. Murali, J.L. Marguerite Rupp, Micro-solid state energy conversion membranes: influence of doping and strain on oxygen ion transport and near order for electrolytes, *J Mater Chem A Mater* 5 (2017) 3900–3908, <https://doi.org/10.1039/c6ta09035d>.
- [5] S. Sanna, V. Esposito, A. Tebano, S. Licoccia, E. Traversa, G. Balestrino, Enhancement of ionic conductivity in sm-doped ceria/yttria-stabilized zirconia heteroepitaxial structures, *Small* 6 (2010) 1863–1867, <https://doi.org/10.1002/sml.200902348>.
- [6] S. Sanna, V. Esposito, M. Christensen, N. Pryds, High ionic conductivity in confined bismuth oxide-based heterostructures, *APL Mater.* 4 (2016), <https://doi.org/10.1063/1.4971801>.
- [7] S. Sanna, V. Esposito, J.W. Andreasen, J. Hjelm, W. Zhang, T. Kasama, S. B. Simonsen, M. Christensen, S. Lindererth, N. Pryds, Enhancement of the chemical stability in confined δ -Bi₂O₃, *Nat. Mater.* 14 (2015) 500–504, <https://doi.org/10.1038/nmat4266>.
- [8] J.S. Sim, J. Shi, S. Ramanathan, Ultra-thin free-standing ceria membranes: layer transfer techniques and high temperature conductivity studies, *J Mater Chem A Mater* 2 (2014) 19019–19028, <https://doi.org/10.1039/c4ta02113d>.
- [9] D. Lu, D.J. Baek, S.S. Hong, L.F. Kourkoutis, Y. Hikita, H.Y. Hwang, Synthesis of free-standing single-crystal perovskite films and heterostructures by etching of sacrificial water-soluble layers, *Nat. Mater.* 15 (2016) 1255–1260, <https://doi.org/10.1038/nmat4749>.
- [10] D. Ji, S. Cai, T.R. Paudel, H. Sun, C. Zhang, L. Han, Y. Wei, Y. Zang, M. Gu, Y. Zhang, W. Gao, H. Huan, W. Guo, D. Wu, Z. Gu, E.Y. Tsymlal, P. Wang, Y. Nie, X. Pan, Free-standing crystalline oxide perovskites down to the monolayer limit, *Nature* 570 (2019) 87–90, <https://doi.org/10.1038/s41586-019-1255-7>.
- [11] J. Bouaziz, C. Cancellieri, B. Rheingans, L.P.H. Jeurgens, F. la Mattina, Advanced Epitaxial Lift-Off and Transfer Procedure for the Fabrication of High-Quality Functional Oxide Membranes, *Adv Mater Interfaces* (2022), 2201458, <https://doi.org/10.1002/admi.202201458>.
- [12] Y. Li, C. Xiang, F.M. Chiabrera, S. Yun, H. Zhang, D.J. Kelly, R.T. Dahm, C.K. R. Kirchert, T.E.L. Cozannet, F. Trier, D.V. Christensen, T.J. Booth, S.B. Simonsen, S. Kadkhodazadeh, T.S. Jespersen, N. Pryds, Stacking and Twisting of Free-standing Complex Oxide Thin Films, *Advanced Materials* (2022), <https://doi.org/10.1002/adma.202203187>.
- [13] V. Esposito, E. Traversa, Design of electroceramics for solid oxides fuel cell applications: playing with ceria, *Journal of the American Ceramic Society* 91 (2008) 1037–1051, <https://doi.org/10.1111/j.1551-2916.2008.02347.x>.
- [14] T.L. Skafte, Z. Guan, M.L. Machala, C.B. Gopal, M. Monti, L. Martinez, E. Stamate, S. Sanna, J.A. Garrido Torres, E.J. Crumlin, M. García-Melchor, M. Bajdich, W. C. Chueh, C. Graves, Selective high-temperature CO₂ electrolysis enabled by oxidized carbon intermediates, *Nat Energy* 4 (2019) 846–855, <https://doi.org/10.1038/s41560-019-0457-4>.
- [15] X. Sun, M. Chen, S.H. Jensen, S.D. Ebbesen, C. Graves, M. Mogensen, Thermodynamic analysis of synthetic hydrocarbon fuel production in pressurized solid oxide electrolysis cells, *Int. J. Hydrogen Energy* 37 (2012) 17101–17110, <https://doi.org/10.1016/j.ijhydene.2012.08.125>.
- [16] S. Sanna, V. Esposito, D. Pergolesi, A. Orsini, A. Tebano, S. Licoccia, G. Balestrino, E. Traversa, Fabrication and electrochemical properties of epitaxial samarium-doped ceria films on SrTiO₃-buffered MgO substrates, *Adv. Funct. Mater.* 19 (2009) 1713–1719, <https://doi.org/10.1002/adfm.200801768>.
- [17] A. Kumar, S. Jesse, A. Morozovska, E. Eliseev, A. Tebano, N. Yang, S.v. Kalinin, Erratum: variable temperature electrochemical strain microscopy of Sm-doped ceria (*Nanotechnology* (2013) 24 (145401)), *Nanotechnology* 25 (2014), <https://doi.org/10.1088/0957-4484/25/8/089501>.
- [18] K. Dunnett, A. Narayan, N.A. Spaldin, A.v. Balatsky, Strain and ferroelectric soft-mode induced superconductivity in strontium titanate, *Phys. Rev. B* 97 (2018), <https://doi.org/10.1103/PhysRevB.97.144506>.
- [19] J.P. Ruf, Y. Paik, N.J. Schreiber, H.P. Nair, L. Miao, J.K. Kawasaki, J.N. Nelson, B. D. Faeth, Y. Lee, B.H. Goodge, B. Pamuk, C.J. Fennie, L.F. Kourkoutis, D.G. Schlom, K.M. Shen, Strain-stabilized superconductivity, *Nat. Commun.* 12 (2021), <https://doi.org/10.1038/s41467-020-20252-7>.